



Electron blocking and hole extraction by a dual-function layer for hematite with enhanced photoelectrocatalytic performance

Shuai Chen^a, Jinhua Li^a, Jing Bai^{a,*}, Ligang Xia^a, Yan Zhang^a, Linsen Li^a, Qunjie Xu^{b,d}, Baoxue Zhou^{a,c,d,*}

^a School of Environmental Science and Engineering, Shanghai Jiao Tong University, No. 800, Dongchuan Rd, Shanghai 200240, PR China

^b College of Environmental and Chemical Engineering, Shanghai University of Electric Power, No.2588 Changyang Road, Shanghai, 200090, PR China

^c Key Laboratory of Thin Film and Microfabrication Technology (Ministry of Education), Shanghai 200240, PR China

^d Shanghai Institute of Pollution Control and Ecological Security, Shanghai 200092, PR China

ARTICLE INFO

Keywords:

Fe₂O₃/ZnFe₂O₄/ZnO layer

Electron blocking effect

Hole extraction effect

Photoelectrocatalytic

ABSTRACT

To address the poor charge transport performance and severe surface combination of Hematite (Fe₂O₃), surface modification of electron blocking layer with a more negative conduction band than Fe₂O₃ have gradually received attention, which could prevent excess electrons escaping from Fe₂O₃ to the electrode surface. However, the electron blocking process is often accompanied by the similar hole blocking effect, resulting in severe secondary interface recombination. Here, we design a ZnFe₂O₄ active layer between Fe₂O₃ substrate and ZnO electron blocking layer to avoid the interface stacking phenomenon of photogenerated carriers. The photo-generated holes can be promptly extracted from valence band of Fe₂O₃ to the photoanode surface and the electrons can be smoothly delivered from Fe₂O₃ and FTO, avoiding the carriers interface accumulation. The optimized Fe₂O₃/ZnFe₂O₄/ZnO achieved a significant enhancement in photocurrent of 0.805 mA/cm² at 1.23 V vs. RHE when compared to the pristine Fe₂O₃ value of 0.12 mA/cm², Fe₂O₃/ZnFe₂O₄ of 0.58 mA/cm² and Fe₂O₃/ZnO of 0.38 mA/cm², increased by 670%, 140% and 210%, respectively. Meanwhile, the degradation rate constant is remarkably increased by 483%, 144% and 191% for treating a typical organic pollutant of methyl orange. Our finding emphasizes the importance of electron blocking layer and holes extraction layer on overall photogenerated carriers' transfer, in achieving a hematite based photoanode with high PEC performance. These results provide a new strategy toward the surface design of more efficient PEC water splitting and organic degradation photoanode.

1. Introduction

Hematite (Fe₂O₃) has been standing out as one of the most promising semiconductor material for photoelectrocatalytic (PEC) reaction by integrating its good light absorption, suitable band structure, low-cost and thermodynamically stability [1–4]. This unique combination of hematite can theoretically ensure the efficient conversion of light energy, whereas the reality is pale that efforts to prepare superior hematite photoanode have been unsuccessful [5]. Its actual activity is far below the theoretical value mainly because of poor charge carrier transport performance and slow surface reaction kinetics [6,7]. Poor charge carrier transfer efficiency often leads to severe electron-hole recombination in bulk Fe₂O₃ and at the electrode surface. Ion doping is considered as one of the most common approach to improve charge transport [8,9]. Some researchers built a bulk band bending of Fe₂O₃ via gradient doping modification, which favors the substantially

reduction of bulk recombination [10–12]. However, the exact nature of doping for photoelectrode stability is still unclear. Another main approach to enhance charges transfer efficiency is surface modifications [13–16]. To obtain a low surface electron-hole recombination and high hole collection efficiency in the hematite photoelectrode, most of surface modifications focused on employing functional overlayers such as TiO₂, ZnO, Nb₂O₅ [7,17,18]. These ultrathin overlayers possess suitable conduction band edge positions compared to Fe₂O₃ which are beneficial to electron transfer and suppressing electron-hole recombination at the electrolyte/hematite interface [14]. However, the role of the overlayer that acts as a blocking layer was not investigated in detail in these studies. Additionally, slow surface reaction kinetics is also the key issue which limits the PEC performance of Fe₂O₃ [19]. In order to overcome this defect, a large overpotential is often necessary to suppress the surface recombination. As a result, numerous holes accumulate on the surface, which causes the electron photogenerated near the

* Corresponding authors at: School of Environmental Science and Engineering, Shanghai Jiao Tong University, Shanghai 200240, PR China.

E-mail addresses: bai_jing@sjtu.edu.cn (J. Bai), zhoubaoxue@sjtu.edu.cn (B. Zhou).

<https://doi.org/10.1016/j.apcatb.2018.05.068>

Received 5 February 2018; Received in revised form 17 May 2018; Accepted 24 May 2018

Available online 25 May 2018

0926-3373/© 2018 Elsevier B.V. All rights reserved.

surface leaking to the electrode surface and further the severe surface recombination. Thus a functional electron blocking layer for hematite is essential to reach a better surface charge transfer and separation efficiency.

Based on the above two aspects, surface electron engineering implemented by an overlayer modification could efficient prevent excessive electrons escaping to the surface and suppressing electron–hole recombination at the electrolyte/hematite interface. What we need is a transparent and stable metal oxide overlayer encapsulated hematite such as ZnO which contains a stable and sufficiently negative conduction band compared to the hematite. For example, Xi et al. formed a ZnO passivation layer on top of Fe_2O_3 film, changing the flat band potential of hematite and reduces the surface defects [17]. However, since the valence band of the Fe_2O_3 is relative higher than most of the semiconductor oxides, the electron blocking process is often accompanied by the similar hole blocking effect that thicker overlayer (> 20 nm) also prevents hole transport to the surface, resulting in severe hole accumulation at the interface between Fe_2O_3 and the overlayer. Consequently, serious secondary interface recombination will occur coupled with the stack of blocked electron. Therefore, not only controlling the thickness of overlayer, but also seeking an appropriate active layer that could avoid the interface stacking phenomenon of photogenerated carriers between Fe_2O_3 and the overlayer, is imperative. We noticed on the ferrite-based semiconductor (ZnFe_2O_4), a chemically stable n-type narrow bandgap semiconductor (1.9–2.0 eV) with suitable band position for Fe_2O_3 , which also ameliorates the poor conductivity of Fe_2O_3 [20–23]. Importantly, ZnFe_2O_4 is a stable product of Fe_2O_3 and ZnO via high temperature solid state reaction. Theoretically, a further enhancement is possible through the insertion of active ZnFe_2O_4 layer. On the one hand, active ZnFe_2O_4 layer could extract the stacked holes from Fe_2O_3 and favor the hole flow to tunnel through the ZnO overlayer to reach the surface and electrolyte; and on the other hand, deliver the excess electrons to Fe_2O_3 and FTO and avoid the electrons accumulation near the interface. Interestingly, a planar $\text{Fe}_2\text{O}_3/\text{ZnO}$ or $\text{Fe}_2\text{O}_3/\text{ZnFe}_2\text{O}_4$ performs poorly without the third component based on the roughly the same PEC performance of Fe_2O_3 [20,24]. This situation indicated that both ZnO and ZnFe_2O_4 overlayer is vital for fabricating a high performance Fe_2O_3 photoanode through charge carriers engineering.

Therefore, we followed the idea of *in situ* solid reaction to build a triple heterojunction photoelectrode consisting of Fe_2O_3 substrate, ZnFe_2O_4 hole extraction layer and ZnO electron blocking layer (Fig. 1A). The triple-layer photoanode was fabricated via *in situ* reaction of ZnAc and electro-reduced Fe film under once thermal treatment, in which Fe film was oxidized into Fe_2O_3 film and $\text{ZnFe}_2\text{O}_4/\text{ZnO}$ layer was generated simultaneously on the surface of Fe_2O_3 , followed by the soaking process in KOH to remove the excess ZnO. Because the amount

of ZnO is expected to have great impact to the PEC performance of photoanode, ZnO overlayer was optimized by tuning soaking time. This unique homogeneous three-phase structure can be a good way to overcome the defects of multiple calcinations to form multi-phase structure. By inserting additional ZnFe_2O_4 and reducing the thickness of surface ZnO, the prepared photoanode shows a significantly enhanced photocurrent of $0.805 \text{ mA}/\text{cm}^2$ at 1.23 V vs. RHE compared to the separate deposition of ZnFe_2O_4 or ZnO as well as pristine hematite. Meanwhile, the degradation rate constant is remarkably increased. Electron-blocking effect of ZnO and holes-extraction effect of ZnFe_2O_4 are the major two beneficial roles. This synergistic effect of ZnFe_2O_4 and ZnO over hematite accelerates charge transfer and avoids loss of charge across the hematite/electrolyte interface (Fig. 1B).

2. Results and discussion

2.1. Synthesis and characterization of $\text{Fe}_2\text{O}_3/\text{ZnFe}_2\text{O}_4/\text{ZnO}$ photoanode

An *in situ* solid-state reaction mechanism was employed to naturally fabricate the hematite photoanode co-coated with $\text{ZnFe}_2\text{O}_4/\text{ZnO}$ layer. In order to facilitate the growth of $\text{ZnFe}_2\text{O}_4/\text{ZnO}$ layer, a compact and orderly Fe_2O_3 planar substrate was adopted [6] (Figure S1). The surface modification involved firstly a little amount of ZnAc coated over electrodeposited Fe film. The different spin-coating layers (1–5) mainly control the total volume of Zn element. Zn-treatment results in a much rougher surface than pristine hematite (Figure S2). After high temperature solid reaction, the triple phase heterojunction is fabricated. And the last process that soaking in KOH is to regulate the outmost ZnO by tuning the dipping time (Figure S2). Noteworthy, the samples with 8 and 12 h were extracted as main object, denoting as $\text{Fe}_2\text{O}_3/\text{ZnFe}_2\text{O}_4/\text{ZnO}$ and $\text{Fe}_2\text{O}_3/\text{ZnFe}_2\text{O}_4$ respectively. As control, the naked $\text{Fe}_2\text{O}_3/\text{ZnO}$ and Fe_2O_3 were also prepared by control the thermal reaction conditions and soaking time, respectively.

XRD and XPS were used to track the formation of ZnFe_2O_4 in the solid-phase reaction of Fe and ZnAc as well as the trace of ZnO during the soaking process. Fig. 2A shows the X-ray diffraction (XRD) of pristine Fe_2O_3 , $\text{Fe}_2\text{O}_3/\text{ZnFe}_2\text{O}_4/\text{ZnO}$, $\text{Fe}_2\text{O}_3/\text{ZnFe}_2\text{O}_4$, and $\text{Fe}_2\text{O}_3/\text{ZnO}$. The pure Fe_2O_3 crystallized in the hexagonal phase (JCPDS 33-0664) as evidenced by the appearance of diffraction peaks (012), (104), (110) without other impure phase characteristic peaks been detected. It is obviously that an additional peak of ZnFe_2O_4 appeared after ZnAc deposited ($\text{Fe}_2\text{O}_3/\text{ZnFe}_2\text{O}_4/\text{ZnO}$ and $\text{Fe}_2\text{O}_3/\text{ZnFe}_2\text{O}_4$), which is in accordance with the (220) plane (JCPDS 22–1012). As we expect, the signal of ZnO is observed in the samples of $\text{Fe}_2\text{O}_3/\text{ZnFe}_2\text{O}_4/\text{ZnO}$ and $\text{Fe}_2\text{O}_3/\text{ZnO}$. Additionally, both weaker characteristic peak of ZnFe_2O_4 and the stronger of ZnO mean a small amount of ZnFe_2O_4 is formed as respect to un-solid-reacted ZnO. Besides, XRD spectra with different

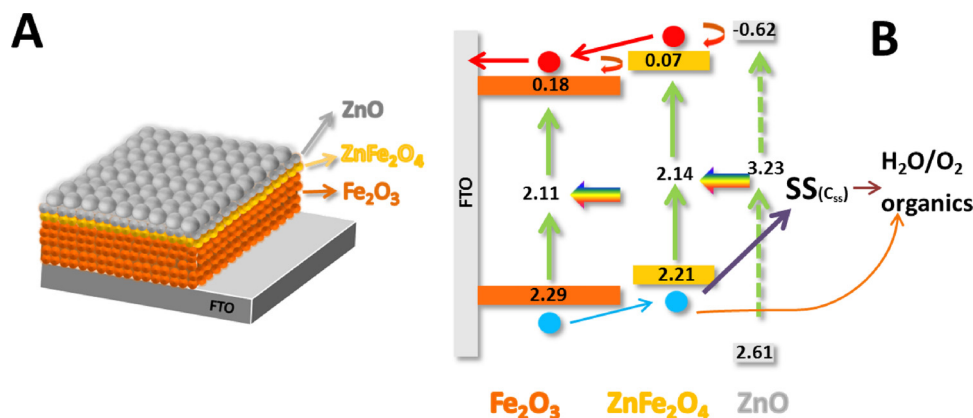


Fig. 1. (A) Schematic image showing the structure of the final $\text{Fe}_2\text{O}_3/\text{ZnFe}_2\text{O}_4/\text{ZnO}$ photoanode. (B) Schematic for the Energy Band Structure of $\text{Fe}_2\text{O}_3/\text{ZnFe}_2\text{O}_4/\text{ZnO}$ photoanode. The energy band position is calculated and confirmed by UPS (Figure S14) and UV (Fig. 2B and Figure S15) spectra.

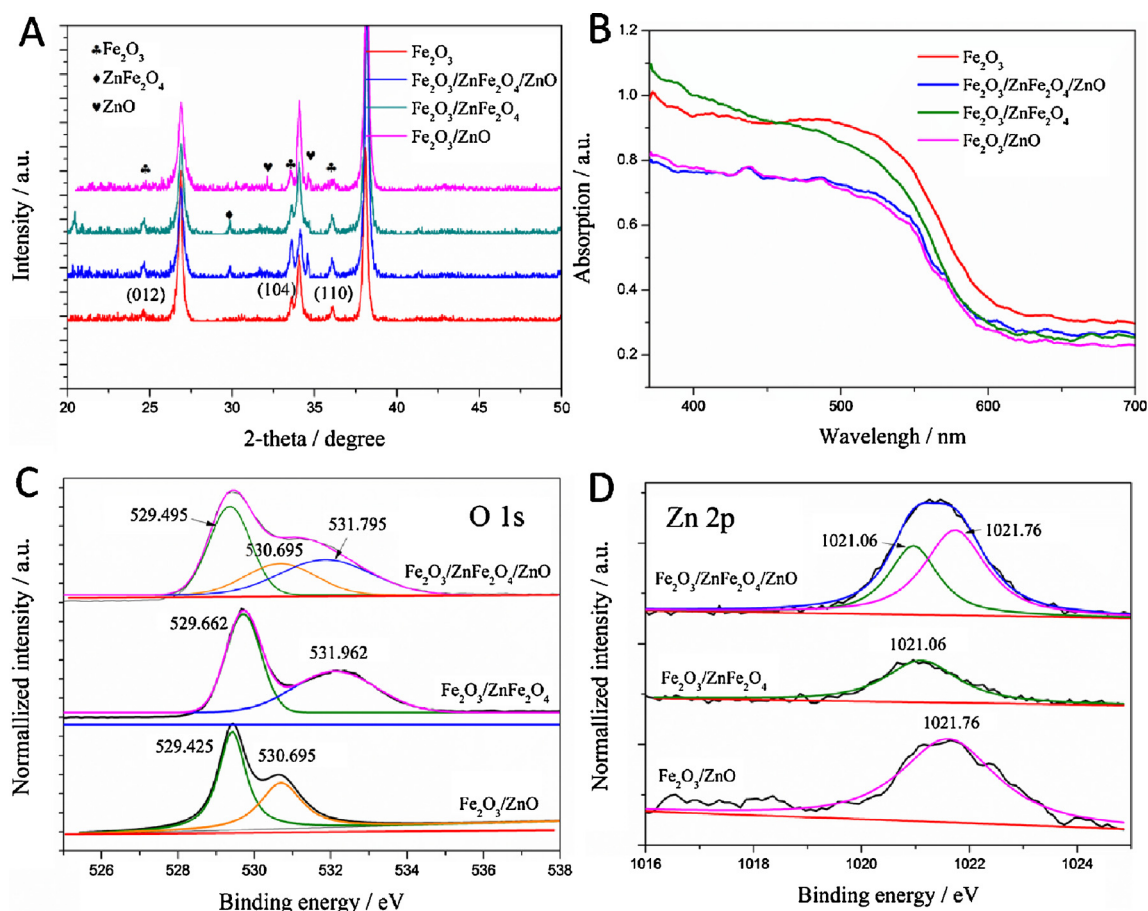


Fig. 2. XRD (A) and UV-vis absorption (B) spectra of Fe₂O₃, Fe₂O₃/ZnFe₂O₄/ZnO, Fe₂O₃/ZnFe₂O₄, and Fe₂O₃/ZnO. O 1s (C) and Zn 2p (D) core-level spectra of Fe₂O₃/ZnFe₂O₄/ZnO, Fe₂O₃/ZnFe₂O₄, and Fe₂O₃/ZnO.

soaking time illustrated the existence of ZnO for 8 h, and decreased for further soaking process until 12 h (Figure S3). Unsurprisingly, no clear peaks from ZnFe₂O₄ appeared seen in Fe₂O₃/ZnO.

Due to the shortage of XRD surface analysis, x-ray photoelectron spectroscopy (XPS) was used to further probe mainly the surface of the films. The full scan spectrum shown in Figure S4 reveals the presence of the same elements include Fe, Zn and O except impurity C on the surface of Fe₂O₃/ZnFe₂O₄/ZnO. The O 1s spectrum for Fe₂O₃/ZnFe₂O₄ contains two compositions located at 529.662 and 531.962 eV, which could be attributed to the O distributed in Fe₂O₃ and ZnFe₂O₄ in consistent with XRD [22]. Compared to the sample of Fe₂O₃/ZnFe₂O₄, Fe₂O₃/ZnFe₂O₄/ZnO shows another peak at bind energy of 530.695 eV which accounts for the existence of ZnO [25], as already evinced for XRD mentioned above. Besides, Zn 2p orbit also illustrates this point due to the additional shoulder that located at higher band energy of 1021.76 eV on fitting curve of Fe₂O₃/ZnFe₂O₄/ZnO compared to the sample of Fe₂O₃/ZnFe₂O₄. The peak at 1021.76 eV is a signal coming from un-solid-reaction ZnO [25]. After 12 h of soaking treatment, the Zn 2p3/2 peak of Fe₂O₃/ZnFe₂O₄ narrowed as shown in Fig. 2D, indicating the reduction of Zn-based compounds on the surface. Both the spectra of XRD and XPS showed the situation that the coexistence of excess ZnO and ZnFe₂O₄ as well as the non-existence of ZnO for Fe₂O₃/ZnFe₂O₄ and ZnFe₂O₄ for Fe₂O₃/ZnO.

Upon UV-vis light absorption, the presence of ZnO in both Fe₂O₃/ZnFe₂O₄/ZnO and Fe₂O₃/ZnO significantly reduce the light absorption, maybe due to the large bandgap of ZnO leading to the substantial reduction of visible light region absorption although the thickness is very thin [24]. Additionally, a smaller absorption coefficient of ZnFe₂O₄ than that of Fe₂O₃ slightly decreases the absorption of high wavelength

spectra for the sample of Fe₂O₃/ZnFe₂O₄/ZnO. Therefore, the improvement of photocurrent for Fe₂O₃/ZnFe₂O₄/ZnO is not ascribed to the increased light absorption.

To obtain a deeper evidence of morphology in surface, we performed SEM and TEM with as-formed samples. The SEM images exhibit a similar morphology with compact surface consisted of nanoparticles (Fig. 3A, B, C and D). Seen in Fig. 3B, the particles of Fe₂O₃/ZnFe₂O₄/ZnO became more evident and full after ZnAc treatment, which enhanced the surface area and formed a nanoporous structure, due to the solid phase reaction and soaking process that reconstructed the surface state (Figure S2). After soaking process for 12 h seen in Fig. 3C, nanoparticles became compact maybe because the further alkali treatment destroyed the nanosphere. The morphology of Fe₂O₃/ZnO remained similar to that of Fe₂O₃/ZnFe₂O₄/ZnO that the nanoparticles with a diameter of ~50 nm became more obvious compared to pristine hematite. The thicknesses of all prepared samples remain constant of about 180 nm, indicating the only a tiny volume of Zn-based compounds was deposited on the surface of Fe₂O₃, as confirmed by EDX shown in Figure S5.

As observed through the TEM images of ZnAc treatment samples, an obvious finer spherical structure is presented in Fig. 4B, C and D, whereas the surface of bare hematite is relatively flat (Fig. 4A and Figure S1). Fig. 4B, C and D are the TEM images of Fe₂O₃/ZnFe₂O₄/ZnO, Fe₂O₃/ZnFe₂O₄ and Fe₂O₃/ZnO respectively, demonstrating that nanosphere with diameter of around 20 nm is uniformly distributed at the surface. The HRTEM images (right side) were extracted with typical characteristics from original background image (left side). In Fig. 4B', it is visible that ZnO and ZnFe₂O₄ coexist in a separate nanosphere while ZnFe₂O₄ located inside, in line with the law of interface reaction. On

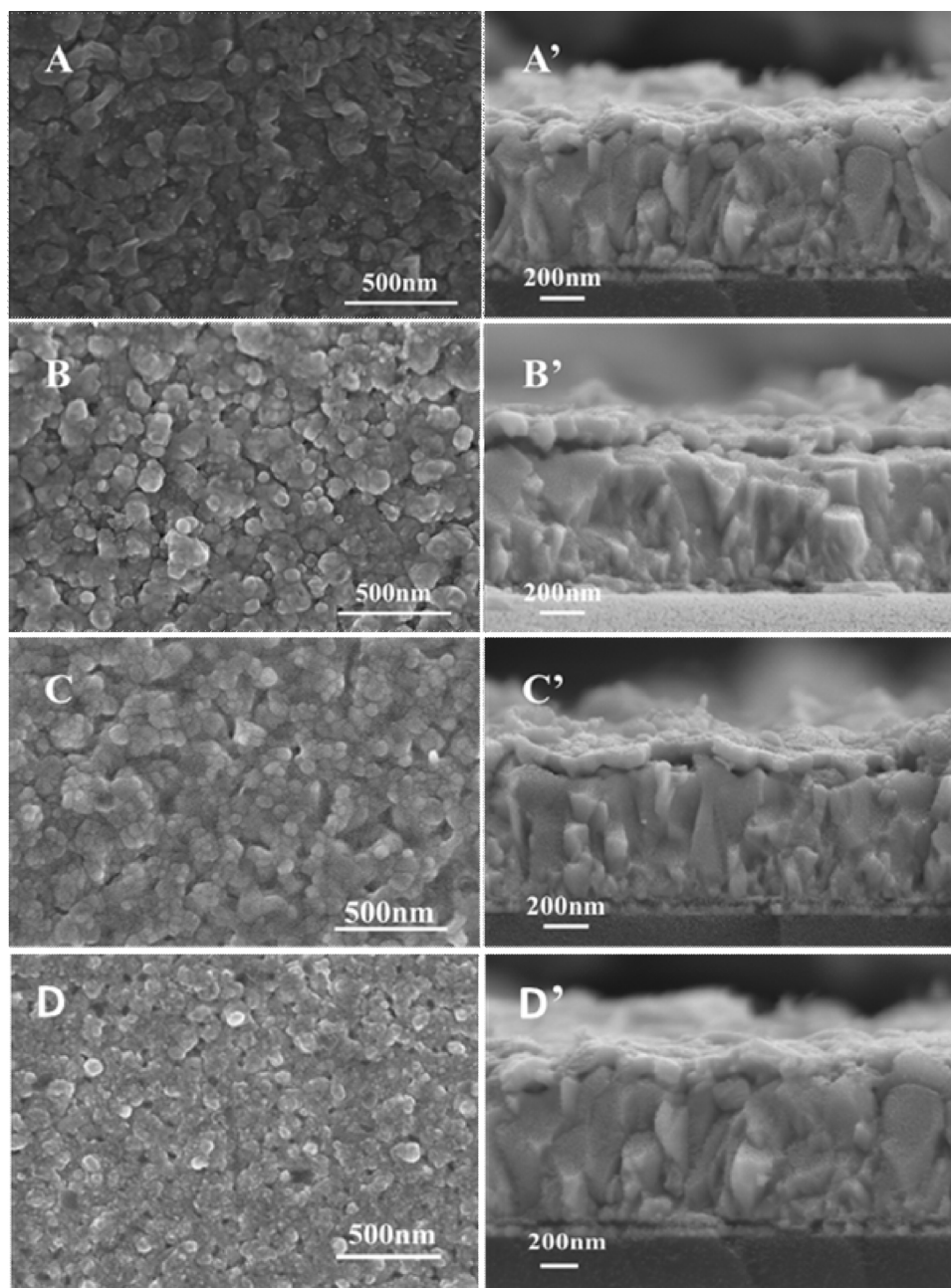


Fig. 3. SEM images of Fe_2O_3 (A and A'), $\text{Fe}_2\text{O}_3/\text{ZnFe}_2\text{O}_4/\text{ZnO}$ (B and B'), $\text{Fe}_2\text{O}_3/\text{ZnFe}_2\text{O}_4$ (C and C') and $\text{Fe}_2\text{O}_3/\text{ZnO}$ (D and D').

the other hand, the solid reaction of Fe and ZnAc build a compact contact at the interface, making charge transfer more efficiently. In contrast to B', as we expected, ZnFe_2O_4 forms a nanosphere alone without extra ZnO covered in Fig. 4C'. And the image of $\text{Fe}_2\text{O}_3/\text{ZnO}$ (Fig. 4D') illustrated a similar situation like Fig. 4C' that ZnO coating on bare hematite without interfacial ZnFe_2O_4 , excluding the interference of ZnFe_2O_4 . The lattice distance of 0.298 nm and 0.261 nm matched well with the (220) and (002) planes of ZnFe_2O_4 and ZnO in accordance with XRD spectra at $2\theta = 29.88$ and 34.63 , respectively.

2.2. PEC performance of $\text{ZnFe}_2\text{O}_4/\text{ZnO}$ layer coating on Fe_2O_3

The PEC activities of different photoanodes were firstly examined by measuring the photocurrent density for water oxidation in 1 M KOH electrolyte. As-prepared photoanode was optimized in terms of ZnAc spin-coating layer (Figure S6). Figure S6 (A) shows the photoresponses of 1 to 5- $\text{Fe}_2\text{O}_3/\text{ZnFe}_2\text{O}_4$ and pristine hematite without soaking process.

It's no doubt that the deposition of ZnAc significantly enhances the photocurrent. As the coating layer of ZnAc is increased from 1 to 4, the photocurrent increases from 0.08 mA cm^{-2} up to 0.4 mA cm^{-2} at 1.23 V vs RHE, decreasing again at larger coating layer. With different soaking time for 4 h, 8 h and 12 h illustrated in Figure S6(B–D), the photoresponses of different samples all show similar tendency that 4- $\text{Fe}_2\text{O}_3/\text{ZnFe}_2\text{O}_4$ has always been a leader. Concerning the time parameters, the photocurrent value of 4- $\text{Fe}_2\text{O}_3/\text{ZnFe}_2\text{O}_4$ at 1.23 V vs RHE in different soaking time was collected illustrated in Figure S7 (blue line), showing a clear mountain-like pattern that we could find a peak in the point of 8 h. The rest of samples are also roughly the same (Figure S1). Hence, $\text{Fe}_2\text{O}_3/\text{ZnFe}_2\text{O}_4/\text{ZnO}$ with 4 spin-coating layer and 8 h of soaking process is the optimal sample.

Fig. 5A shows the photoresponses of different combinations prepared by different preparation methods. As-prepared Fe_2O_3 photoanode exhibits an onset potential of 1.0 V_{RHE}, and the photocurrent density increases slowly to 0.12 mA cm^{-2} at 1.23 V_{RHE}. After ZnO individually

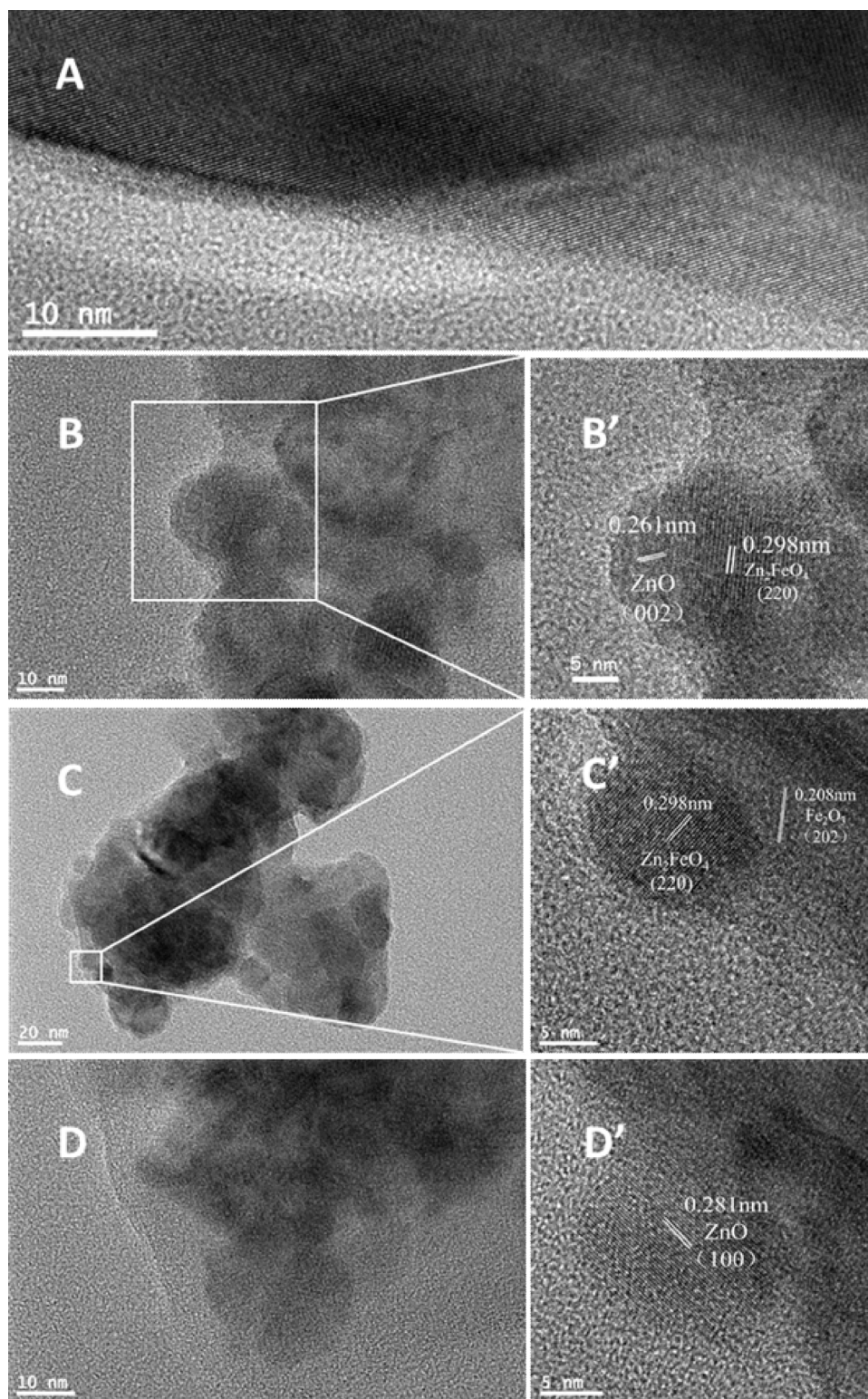


Fig. 4. TEM images of Fe₂O₃ (A), Fe₂O₃/ZnFe₂O₄/ZnO (B and B'), Fe₂O₃/ZnFe₂O₄ (C and C') and Fe₂O₃/ZnO (D and D'). B', C' and D' are the high resolution images corresponding to B, C and D.

decorated Fe₂O₃, the photocurrent density is significantly enhanced at the range from 0.8 to 1.7 V_{RHE}, achieving a photocurrent density of 0.38 mA cm⁻² at 1.23 V_{RHE}. Notably, the insertion of additional ZnFe₂O₄ brings about a dramatic increase in photocurrent density of Fe₂O₃/ZnO up to 0.805 mA cm⁻² at 1.23 V_{RHE}, which increases by 187.5% that of the Fe₂O₃/ZnO. IPCE was also performed to investigate the photoactivity of these samples with respect to the wavelength. Seen

in Fig. 5B, IPCE is consistent with the J–V curves that coexistence of ZnFe₂O₄ and ZnO (blue line) resulted in the highest value of IPCE. These results are in good agreement with photocurrent performance. Furthermore, due to the smaller absorption of Fe₂O₃/ZnFe₂O₄/ZnO and Fe₂O₃/ZnO shown in Fig. 2B, the enhanced IPCE in the region from 350 to 500 nm may be ascribed to the higher separation efficiency rather than increased light absorption.

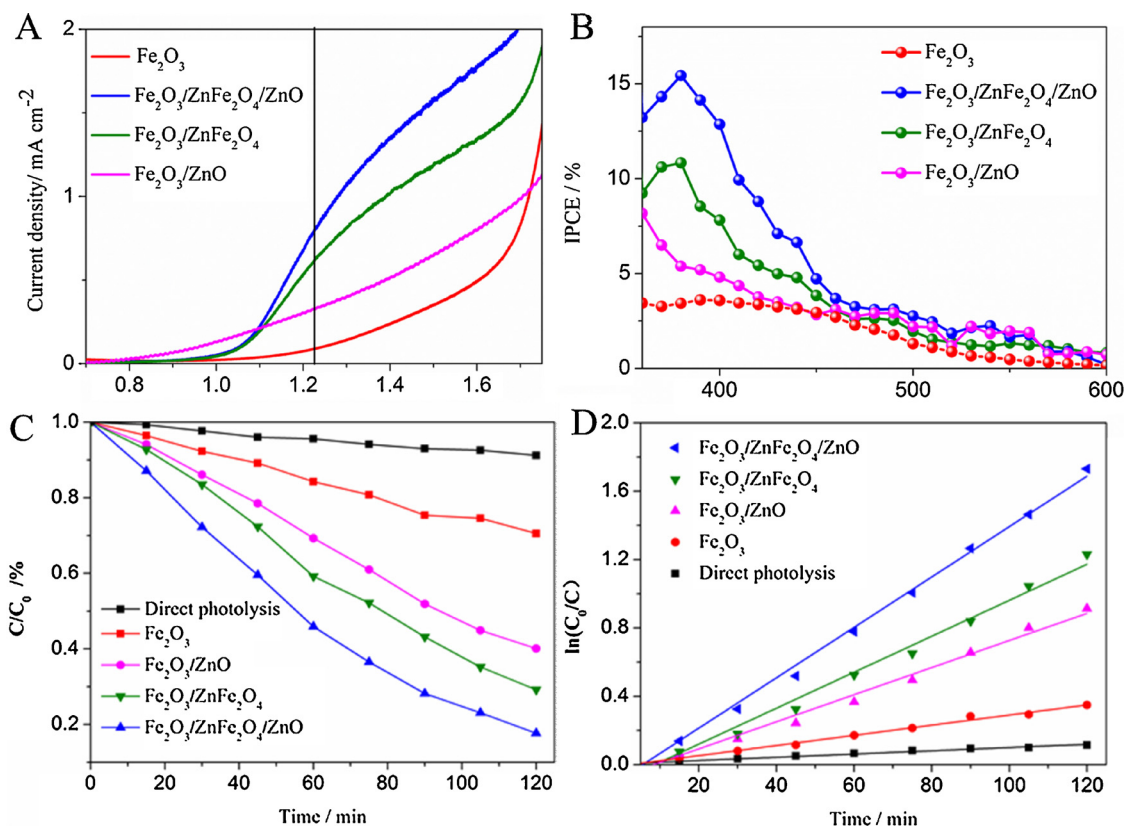


Fig. 5. the photoelectrocatalytic (A), IPCE (B) responses, (C) the degradation (at a bias potential of 1 V vs. Ag/AgCl) and (D) kinetic curves of MO for prepared Fe₂O₃, Fe₂O₃/ZnFe₂O₄/ZnO, Fe₂O₃/ZnFe₂O₄, Fe₂O₃/ZnO and direct photolysis. IPCE and voltammetry measurements Electrolyte: 1 M NaOH. Degradation solution: 0.1 mol L⁻¹ Na₂SO₄ supporting electrolyte and 10 mg L⁻¹ MO, 40 ml. Bias voltage: 1 V vs Ag/AgCl. Illumination: frontside, 100 mW cm⁻², AM 1.5 G.

As seen in figure S11, the I-t curve of 4-Fe₂O₃/ZnFe₂O₄-7 h under alkaline condition shows a trend that rising first until 1 h and then decreasing, which is in line with figure S7 green line. However, the I-t curve of 4-Fe₂O₃/ZnFe₂O₄-7 h under neutral condition shows a totally different current density at 0.6 V vs. Ag/AgCl (1.23 V vs. RHE). The reason may be the oxidation of OH⁻ is known to be more energetically favorable than the oxidation of molecular water (E_{O₂/OH⁻} = 0.401 V and E_{O₂/H₂O} = 1.229 V vs RHE)[26]. Under neutral condition, the amount of OH⁻ is far below the amount of H₂O, so that the photoanode must be at a more positive potential to generate enough oxygen and further reach a sufficiently large current density.

The PEC activities of prepared Fe₂O₃ based photoanodes were simultaneously investigated by degradation experiment of methyl orange (MO). The degradation texts were conducted in neutral aqueous solutions at a bias potential of 1 V vs. Ag/AgCl except the direct photolysis (DP, without a bias potential). The UV-vis absorption was used to measure the concentration of MO at 464 nm. As seen in Fig. 5C, the degradation rate was followed the order of Fe₂O₃/ZnFe₂O₄/ZnO > Fe₂O₃/ZnFe₂O₄ > Fe₂O₃/ZnO > Fe₂O₃ > DP, which is in good agreement with the tendency of photoelectrocatalytic responses [27]. As shown in Fig. 8B, the optimal degradation rate constant is ~0.80541 h⁻¹, which is ~1.44, ~1.91, ~4.83 and ~14.19 times higher than that of Fe₂O₃/ZnFe₂O₄ (~0.5863 h⁻¹), Fe₂O₃/ZnO (~0.4427 h⁻¹), Fe₂O₃ (~0.1748 h⁻¹) and DP (~0.0595 h⁻¹). This indicates that the degradation performance of MO could be improved by coated ZnFe₂O₄ or ZnO on Fe₂O₃, especially the co-coating of ZnFe₂O₄ and ZnO greatly facilitates the degradation process possibly due to the synergies effect of ZnFe₂O₄ and ZnO. For environmental application, the long-term degradation stability of photoanode was detected. As shown in Figure S13, after 3 cycles of degradation, the degradation efficiency of MO was about 74.3%, showing a relatively weak attenuation from 89.8% to 74.3%. The reason may be the

instability of Fe₂O₃ under neutral condition, as confirmed by the attenuation at the beginning operation shown in Figure S11. After 5 cycles operation, the degradation efficiency is stable at 75%, which is in line with the long-term stability shown in Figure S11. This result indicated the property of Fe₂O₃/ZnFe₂O₄/ZnO was stabilized for long-term degradation operation. However, to explain the origin of higher PEC performance needs further studies to investigate the role of ZnFe₂O₄ and ZnO.

2.3. The interface carrier dynamics process affected by surface ZnFe₂O₄/ZnO

Firstly, to investigate the blocking effect of outmost ZnO, we measured the photocurrent densities of pristine Fe₂O₃ and Fe₂O₃/ZnO from frontside (film side) and backside (FTO side) under visible illumination (λ > 400 nm, make sure ZnO is inactive). As illustrated in Figure S8, pristine Fe₂O₃ photoanode shows almost the same photocurrent density under frontside and backside illumination. However, Fe₂O₃/ZnO photoelectrode obtains a significantly higher photocurrent of 0.24 mA cm⁻² at 1.23 V_{RHE} under frontside illumination, which is almost 1.5 times higher than that under backside illumination. For pristine hematite, the similar photocurrent tendency signifies the similar carrier transport efficiency whether near the FTO or the surface. The most reasonable explanation for Fe₂O₃/ZnO might be that the ZnO overlayer blocks electron back into surface and thus the photogenerated charge carrier near the surface could be efficiently separated. Therefore, this electron blocking effect could enhance the carrier separation efficiency in Fe₂O₃[7].

In order to gain insight into the charge transfer and recombination mechanism, electrochemical impedance spectra (EIS) measurements were conducted at different potentials from 0.7 ~ 1.3 V_{RHE}. Fig. 6A shows typical EIS curves at 1.23 V_{RHE}. The minor semicircles at high

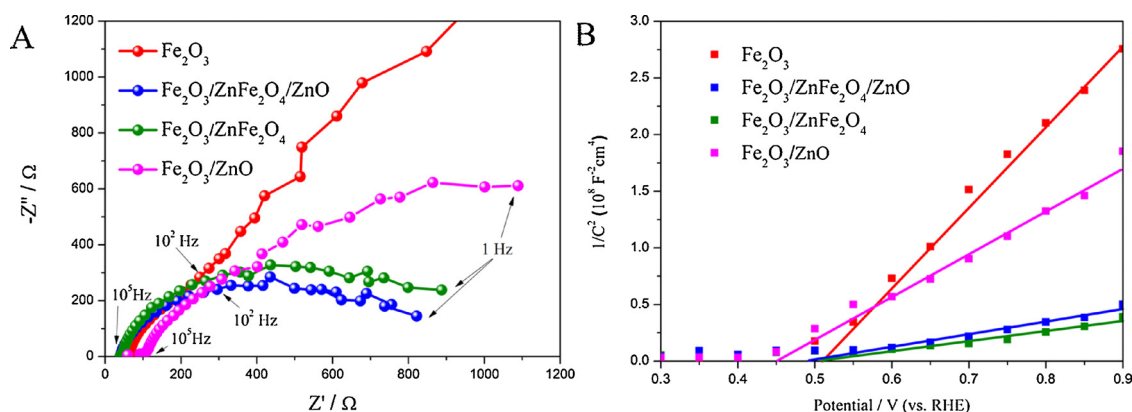


Fig. 6. the Nyquist (A) and Mott-Schottky (B) plots of Fe_2O_3 , $\text{Fe}_2\text{O}_3/\text{ZnFe}_2\text{O}_4/\text{ZnO}$, $\text{Fe}_2\text{O}_3/\text{ZnFe}_2\text{O}_4$ and $\text{Fe}_2\text{O}_3/\text{ZnO}$. Electrolyte: 1 M NaOH. Nyquist plot illumination: frontside, 100 mW cm^{-2} , AM 1.5 G. Mott-Schottky illumination: frontside, dark condition. AC amplitude: 10 mV. Frequency range: 1 Hz–100 MHz.

frequency (10^5 Hz – 10^2 Hz) refer to the carriers transfer resistance in the bulk of electrodes and the major semicircles at low frequency (10^2 Hz –1 Hz) represent the carriers transfer process at the surface states. Obviously, the similar high frequency semicircles and completely different low frequency semicircles indicate the dominant role of surface states due to the surface modification of $\text{ZnFe}_2\text{O}_4/\text{ZnO}$. Unsurprisingly, the co-existence of ZnFe_2O_4 and ZnO results in the lower resistance, exhibiting the faster charge transfer kinetics at the electrode interface thus leading to the higher photocurrent responses (Fig. 5A).

To obtain the further dynamics of carriers at the surface, the EIS data were thus fitted to an equivalent circuit (EC) depicted in Figure S9. The EC contains the carriers trapping and transfer resistances on the surface (R_{trap} , $R_{\text{ct,ss}}$) and the corresponding capacitance in the depletion layer or on the surface (C_{bulk} , C_{ss}). The two parallel circuits represent direct hole transfer (through the valence band, DT) and indirect hole transfer (trapping holes at traps or SSs, IT), respectively [28]. To better realize the ZnO and ZnFe_2O_4 induced photoactivity effects over

hematite, the plots of these parameters vs. applied potential were illustrated in Fig. 7. For bare Fe_2O_3 (red line), C_{bulk} value gradually decreases but the C_{ss} value increases with potential, implying more charge carriers are captured by SS (IT process). The largest values of R_{trap} and $R_{\text{ct,ss}}$ mean the worst interface charge transfer performance among all photoanode. When coupled with ZnO (pink line), a lowest C_{bulk} value and a highest C_{ss} value at $0.7 \text{ V}_{\text{RHE}}$ indicate a larger percentage of charge located on SS instead of depletion layer (IT process), possibly because of the surface passivation and co-catalytic effect of ZnO . However, an increased tendency of C_{bulk} is observed from 0.7 – $0.9 \text{ V}_{\text{RHE}}$, revealing more and more holes accumulated in depletion layer, maybe caused by the unmatched valence band of ZnO . The decreased value of C_{ss} (pink line) also implies the accumulation of depletion layer so that fewer holes are located on SS. The lower R_{trap} and $R_{\text{ct,ss}}$ compared to pristine hematite signify the better interface charge transfer performance. All of these mean outmost ZnO could not only passivate surface of Fe_2O_3 , but also intercept holes transfer from valence band and lead to

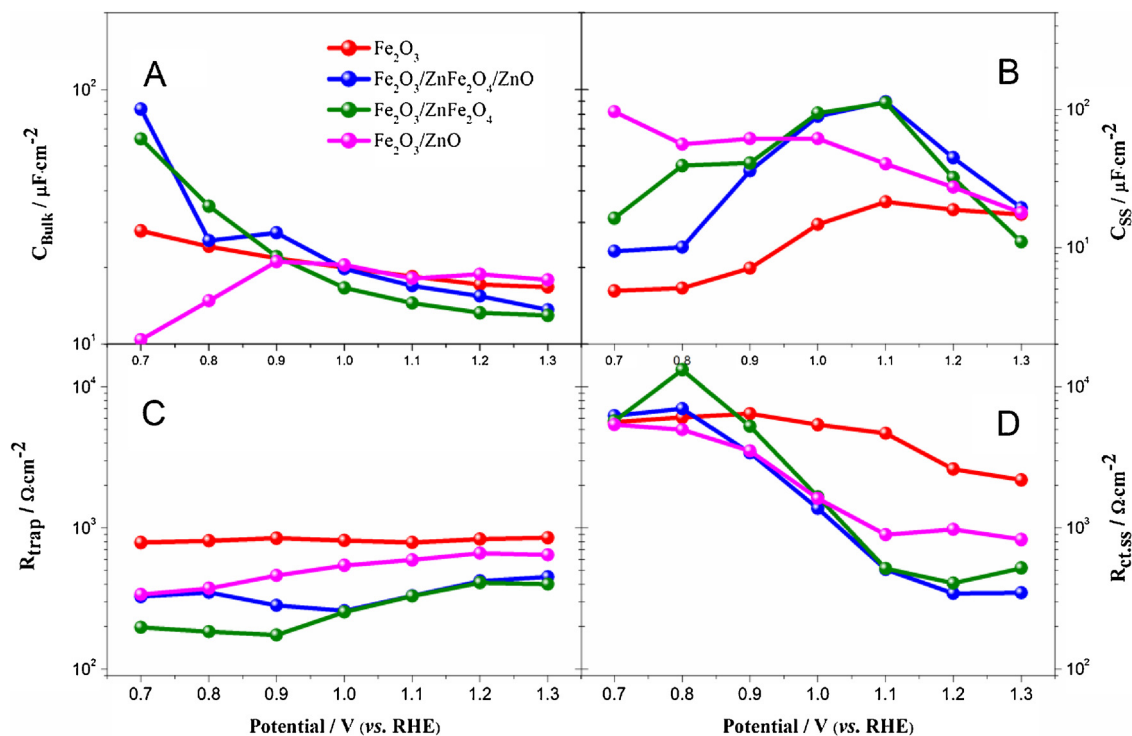


Fig. 7. Capacitances (top) and resistances (bottom) associated with the charge trapping (R_{trap} , C_{bulk}) and transfer ($R_{\text{ct,ss}}$, C_{ss}) at/from SSs with different potentials and different samples (Fe_2O_3 , $\text{Fe}_2\text{O}_3/\text{ZnFe}_2\text{O}_4/\text{ZnO}$, $\text{Fe}_2\text{O}_3/\text{ZnFe}_2\text{O}_4$ and $\text{Fe}_2\text{O}_3/\text{ZnO}$) obtained by fitting their ECs shown in Fig. S5. Error bars stem from the goodness of these fittings, each fitting error does not exceed 10%. Electrolyte: 1 M NaOH. Illumination: frontside, 100 mW cm^{-2} , AM 1.5 G.

transient accumulation.

After the insertion of ZnFe_2O_4 , a completely opposed behavior is observed. At photocurrent onset (0.7–0.9 V_{RHE}), higher values of C_{bulk} and lower values of C_{ss} (blue line) mean a larger percentage of charge transfer from depletion layer rather than SS (DT process). That means ZnFe_2O_4 maybe act as a holes extraction layer to let holes transfer from valence (DT process) rather than SS (IT process). And no accumulation phenomenon on valence band is observed. Concomitantly with the bias potential increased, the activity of SS increased significantly, causing a large number of holes captured on SS (Fig. 6A and B, blue line). At the same time, surface $\text{ZnFe}_2\text{O}_4/\text{ZnO}$ show a better catalytic effect than single ZnO, as mirrored by the lower charge-transfer resistance at the oxygen evolution potential (R_{trap} and $R_{\text{ct,ss}}$, blue line), which are consistent with the J–V curves.

For the further information on the heterojunction bulk, the Mott–Schottky plots were conducted in the dark (Fig. 6B). Due to the inversely proportion of the slope and charge donation density (N_d), the larger the slope is, the lower is the charge density. It is obviously that the plot of $\text{Fe}_2\text{O}_3/\text{ZnO}$ shows lower slope than bare hematite, evincing a higher charge density possibly caused by electron donation from ZnO. In addition, the lower slope of $\text{Fe}_2\text{O}_3/\text{ZnFe}_2\text{O}_4/\text{ZnO}$ suggested a higher charge density mainly due to the formed internal recycle between Fe_2O_3 and ZnFe_2O_4 . Interestingly, almost the same slopes of $\text{Fe}_2\text{O}_3/\text{ZnFe}_2\text{O}_4$ and $\text{Fe}_2\text{O}_3/\text{ZnFe}_2\text{O}_4/\text{ZnO}$ indicate ZnO has nearly no electron transmission to $\text{Fe}_2\text{O}_3/\text{ZnFe}_2\text{O}_4$, which is opposite to $\text{Fe}_2\text{O}_3/\text{ZnO}$. On the other hand, the flat potentials (V_{fb}) of four samples (follow the order of Fe_2O_3 , $\text{Fe}_2\text{O}_3/\text{ZnFe}_2\text{O}_4/\text{ZnO}$, $\text{Fe}_2\text{O}_3/\text{ZnFe}_2\text{O}_4$ and $\text{Fe}_2\text{O}_3/\text{ZnO}$) located on 0.512, 0.495, 0.505 and 0.451 V_{RHE} respectively. A 0.061 V negative shift was achieved by $\text{Fe}_2\text{O}_3/\text{ZnO}$, in line with the lower photocurrent onset shown in Fig. 5A (pink line), confirming that ZnO shift the band edge of Fe_2O_3 to more negative value. However, a tiny negative onset potential shift of $\text{Fe}_2\text{O}_3/\text{ZnFe}_2\text{O}_4/\text{ZnO}$ isn't observed in Fig. 5D (blue line). The reason for these differences may come from different volume of surface ZnO that the amount of ZnO over $\text{Fe}_2\text{O}_3/\text{ZnFe}_2\text{O}_4$ is undoubtedly less than that of $\text{Fe}_2\text{O}_3/\text{ZnO}$. Sufficient amount of ZnO resulted in band edge negative shift and electron donation whereas the ZnO coated on $\text{Fe}_2\text{O}_3/\text{ZnFe}_2\text{O}_4$ could not cause these effects.

Intensity modulated photocurrent spectroscopy (IMPS) was employed to obtain the information about photo-generated electron transport properties. The average transit time (τ), which reflects the recombination probability of photo-generated electrons and holes, can be calculated by the equation $\tau_D = (2\pi f_{\text{min}})^{-1}$, where f_{min} is the frequency at which the minimum value occurs in the IMPS plot. Seen in Fig. 8, the electron transit time, for Fe_2O_3 , $\text{Fe}_2\text{O}_3/\text{ZnFe}_2\text{O}_4/\text{ZnO}$, $\text{Fe}_2\text{O}_3/\text{ZnFe}_2\text{O}_4$ and $\text{Fe}_2\text{O}_3/\text{ZnO}$.

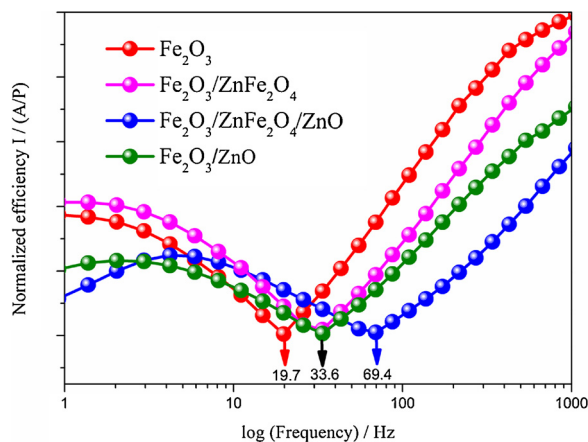


Fig. 8. The IMPS plots of Fe_2O_3 , $\text{Fe}_2\text{O}_3/\text{ZnFe}_2\text{O}_4/\text{ZnO}$, $\text{Fe}_2\text{O}_3/\text{ZnFe}_2\text{O}_4$ and $\text{Fe}_2\text{O}_3/\text{ZnO}$. Electrolyte: 1 M NaOH. Illumination: frontside, 80 mW cm^{-2} , AM 1.5 G. Frequency range: 1 Hz – 1 kHz.

ZnFe_2O_4 and $\text{Fe}_2\text{O}_3/\text{ZnO}$, are calculated to be 8.07, 2.29, 4.74 and 4.76 ms. These results suggest that both ZnFe_2O_4 and ZnO promoted the electron transmission respectively. The barrier layer that ZnO acts as impeded the transportation of charges to the surface and reduced the surface charge recombination (Figure S10). On the other hand, the way of promotion for ZnFe_2O_4 could be attributed to the matched conduction band level to prevent electron accumulation at the interface between Fe_2O_3 and ZnO. This result supports the fact that C_{bulk} is decreasing around the water oxidation potential (0.7 V_{RHE} – 0.9 V_{RHE}) for $\text{Fe}_2\text{O}_3/\text{ZnFe}_2\text{O}_4/\text{ZnO}$ compared to $\text{Fe}_2\text{O}_3/\text{ZnO}$. This means that interface recombination is significantly reduced due to the presence of ZnFe_2O_4 whereas the interface recombination is relatively severe for $\text{Fe}_2\text{O}_3/\text{ZnO}$. Noteworthy, although the amount of ZnO over $\text{Fe}_2\text{O}_3/\text{ZnFe}_2\text{O}_4$ is insufficient to act as electron donation, it could play a vital electron-blocking role to accelerate electron transfer efficiency (Fig. 8, blue line).

2.4. Carriers transfer mechanistic and band diagram model of $\text{ZnFe}_2\text{O}_4/\text{ZnO}$ coating on Fe_2O_3

With this wealth of gathered charge carriers' transfer information, three models of charge transfer process are proposed to account for all the observed phenomenon (Fig. 9). In all cases, the utilized processes of photogenerated holes are divided into two channels including direct hole transfer (DT, orange line) and indirect hole transfer (IT, purple line). For $\text{Fe}_2\text{O}_3/\text{ZnO}$ (Fig. 9A), Fe_2O_3 and ZnO can be both excited to form photogenerated holes and electrons on valence band (VB) and conduction band (CB) respectively under light illumination. Although decorated ZnO can efficiently intercept electron escape to the surface, the unmatched valence band cause severe holes accumulation on the interface, which results in serious interface recombination between Fe_2O_3 and ZnO. Meanwhile, the single ZnFe_2O_4 layer coating on Fe_2O_3 leads to remarkable surface recombination because of the nearer band position of ZnFe_2O_4 and Fe_2O_3 (Fig. 9B). Electrons leak to the photoanode surface resulting striking loss of photogenerated electron, further affecting the overall electron transfer efficiency. For $\text{ZnFe}_2\text{O}_4/\text{ZnO}$ coating on Fe_2O_3 (Fig. 9C), just Fe_2O_3 and ZnFe_2O_4 are excited to generate electron and hole whereas outmost ZnO do not act as a donation layer due to insufficient volume of ZnO. The reason why sufficient holes pass through outmost ZnO to reach the surface is that, 1) outmost ZnO is an ultrathin layer with only ~5 nm as shown in Figure 4B' and 2) the insertion of ZnFe_2O_4 could effectively resolve this hole-blocking defect by effective holes extraction and electron grooming, as confirmed by Fig. 7 (Cbulk and C_{ss}) and Fig. 8. The electron blocking effect of ZnO, coupled with matched conduction band of ZnFe_2O_4 , not only facilitates the electrons flow run orderly, but also efficiently extracts holes to the electrolyte through surface states rather than valence band states. All these conditions effectively suppress the occurrence of interface and surface recombination. Interestingly, the existence of ZnFe_2O_4 promotes a large percentage of holes to be captured by the surface state, which can be explained by the highly active surface group of ZnFe_2O_4 .

3. Conclusion

In summary, we have demonstrated that hematite photoanode with the assistance of electron-blocking effect of outmost ZnO and hole-extraction effect of inserted ZnFe_2O_4 could achieve a significant promoting on PEC water splitting and organic degradation performance. The photogenerated electrons can be efficiently prevented to escape from conduction band to surface, while the photogenerated holes can be promptly extracted from Fe_2O_3 to the surface, avoiding the holes interface accumulation. By varying the number of spin-coating layers and soaking time, the surface ZnFe_2O_4 and ZnO over hematite were optimized, forming the morphology of nanospheres consisting of ZnFe_2O_4 and ZnO. The optimal conditions are 4 coating layer and

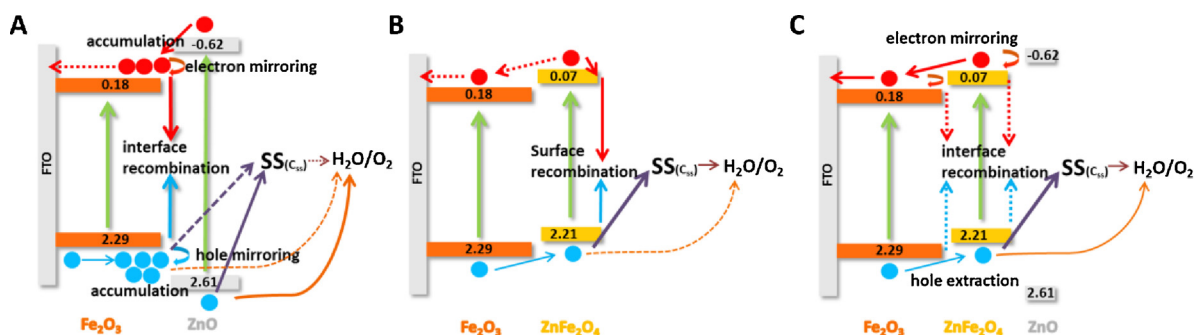


Fig. 9. Schematic representation of proposed charge transport model in $\text{Fe}_2\text{O}_3/\text{ZnO}$ (A), $\text{Fe}_2\text{O}_3/\text{ZnFe}_2\text{O}_4$ (B), and $\text{Fe}_2\text{O}_3/\text{ZnFe}_2\text{O}_4/\text{ZnO}$ (C). The green arrow refers to the charge generation process under light illumination; red circles and blue circles refer to the photogenerated electrons and holes, respectively. Red arrows refer to the electrons transfer and recombination process; blue arrows refer to the holes transfer and recombination process. Purple arrows refer to the indirect process that holes captured by surface states (SS) or surface defect trapping states; orange arrows refer to the direct process that holes transfer through the valence band; dark red arrows refer to the holes transfer to electrolyte from the surface states. (For interpretation of the references to colour in this figure legend, the reader is referred to the web version of this article).

soaking 8 h, respectively. The optimized $\text{Fe}_2\text{O}_3/\text{ZnFe}_2\text{O}_4/\text{ZnO}$ shows high photocurrent density of 0.805 mA cm^{-2} at $1.23 \text{ V}_{\text{RHE}}$ under AM 1.5 irradiation, which increases by 38.7% than that of the $\text{Fe}_2\text{O}_3/\text{ZnFe}_2\text{O}_4$ and 187.5% that of the $\text{Fe}_2\text{O}_3/\text{ZnO}$. ZnO decoration cause severe holes accumulation and interface combination due to the hole-blocking effect of ZnO while single ZnFe_2O_4 results in remarkable surface combination because of electron-escaping effect. The synergy effect of $\text{ZnFe}_2\text{O}_4/\text{ZnO}$ effectively avoided the electron escaping and holes accumulation, further suppressing the surface and interface combination. This work provides a useful insight into the way to improve the charge transfer efficiency for highly effective PEC applications.

4. Experimental

Synthesis of Fe_2O_3 films: The Fe film was first electro-reduced on an F-doped tin oxide (FTO) coated glass substrate ($14 \Omega \text{ cm}^{-1}$) in a two-electrode configuration, with the FTO glass acting as the cathode and a platinum foil as the anode. The distance between the cathode and the anode was 3 cm. The electrolyte was prepared by dissolving 5 g of $\text{FeSO}_4 \cdot 7\text{H}_2\text{O}$ and 30 mL of ammonia (27%) in 150 mL of deionized water, giving a pH of 10.8 at 25°C . The electro-reduced process was conducted at 2 V for 30 s with vigorous stirring. The deposited Fe film was rinsed with deionized water for 5 min and dried at 50°C in a gentle stream of nitrogen for 1 h, followed by thermal oxidation in air at 500°C for 2 h and 720°C for 5 min.

Synthesis of $\text{Fe}_2\text{O}_3/\text{ZnFe}_2\text{O}_4$, $\text{Fe}_2\text{O}_3/\text{ZnFe}_2\text{O}_4/\text{ZnO}$ films: A solution of 20 mM ZnAc in ethanol was spin-coated on as-prepared Fe film. The spin-coating rate was 2000 rpm for 30 s. After that, the ZnAc-treatment Fe films were annealed at 150°C for 3 min. This process was repeated for four cycles. For $\text{Fe}_2\text{O}_3/\text{ZnFe}_2\text{O}_4$ and $\text{Fe}_2\text{O}_3/\text{ZnFe}_2\text{O}_4/\text{ZnO}$, the ZnAc-treatment samples were subsequently annealed at 500°C for 2 h with ramping rates of 1°C min^{-1} to make the ZnAc react at the ZnAc/Fe interface and form ZnFe_2O_4 . $\text{Fe}_2\text{O}_3/\text{ZnFe}_2\text{O}_4$ and $\text{Fe}_2\text{O}_3/\text{ZnFe}_2\text{O}_4/\text{ZnO}$ were finally soaked in 1 M KOH solution for 12 h and 8 h respectively and finally rinsed thoroughly in deionized water to remove the impurities on the surface.

Synthesis of $\text{Fe}_2\text{O}_3/\text{ZnO}$ films: A same solution of 20 mM ZnAc in ethanol was spin-coated on as-prepared Fe_2O_3 film. The spin-coating rate was 2000 rpm for 30 s. After that, the ZnAc-treatment Fe_2O_3 films were annealed at 400°C for 20 min. This process was repeated for four cycles.

Structural characterization: The surface morphology was determined by field emission scanning electron microscopy (FE-SEM; Ultra Plus, Zeiss, Germany). The microstructure and elemental composition were investigated by high-resolution transmission electronic microscopy (HRTEM; Tecnai G2 F30 S-TWIN, FEI, USA). The SEM and TEM both

were equipped with energy-dispersive X-ray detector (EDX). X-ray diffractometry (XRD; AXS-8 Advance, Bruker, Germany) and X-ray photoelectron spectrometry (XPS; AXIS UltraDLD, Kratos, Japan) were applied for structural characterization. Ultraviolet (UV)-vis absorption spectra were recorded on a UV-vis spectrophotometer (TU1900, Beijing Purkinje General Instrument Co, China).

Characterization and photoelectrocatalytic measurements: The PEC water splitting measurements were conducted using a three-electrode system and an electrochemical workstation (CHI 660D, CH Instruments Inc., USA) in 1 M KOH electrolyte. Prior to measurement, the electrolyte was purged with N_2 for 30 min. A platinum foil was used as the auxiliary electrode, and an Ag/AgCl electrode was used as the reference electrode. The light source was a 350-W xenon lamp (Shanghai Hualun Bulb Factory) equipped with an AM 1.5 filter (light density, 100 mW cm^{-2}). The potential scan rate was 50 mV s^{-1} . The measured potentials of the Ag/AgCl electrode were converted to the RHE scale according to the following formula: $E_{\text{RHE}} = E_{\text{Ag/AgCl}} + 0.0591 \times \text{pH} + 0.1976$. The incident photon-to-charge conversion efficiency (IPCE) was measured using a monochromator (Zolix, China) equipped with a 500-W xenon arc lamp, a calibrated silicon photodetector and a power meter. IPCE data were collected from 300 to 700 nm at 1.23 V vs. RHE. Electrochemical impedance spectroscopy (EIS) was performed using the same electrochemical workstation and three-electrode system used for the photocurrent measurements with the following testing conditions: amplitude perturbations of 5 mV, a frequency range of 1 Hz to 10 kHz, and specific direct current constant potentials (0.7–1.3 V vs. RHE). Nyquist plots were fitted to the selected equivalent circuits (ECs) using the Zsimpwin software (v. 3.10). Mott-Schottky plots were obtained from 0 to 2 V vs. RHE at 1 kHz in the dark. Intensity-modulated photocurrent spectroscopy (IMPS) was performed using an electrochemical workstation (Zennium; effect-Elektrik, Germany) coupled with a controlled intensity-modulated photospectroscopy set-up (CIMPS, PP211) and a white-light lamp (WLC02; Zahner-Elektrik) whose DC illumination was adjusted to 80 mW cm^{-2} . The same three-electrode configuration was used. Modulated light in the frequency range of 0.1–10 kHz was applied. The PEC degradation experiment of MO was performed under the following conditions: pH 7 (0.1 mol L^{-1} sodium sulphate supporting electrolyte), AM 1.5 irradiation, vigorous stirring, and bias 1 V vs. Ag/AgCl. The initial concentration of the MO solution was 10 mg L^{-1} with 40 mL of reaction solution. The reaction solution was investigated using a UV-vis spectrophotometer (UV2102 PCS, UNICO, Shanghai).

Acknowledgements

The authors are grateful for financial support provided by the National Nature Science Foundation of China (No. 21576162, No.

51578332, No. 21507085) and SJTU-AEMD for support.

Appendix A. Supplementary data

Supplementary material related to this article can be found, in the online version, at doi:<https://doi.org/10.1016/j.apcatb.2018.05.068>.

References

- [1] K. Sivula, F. Le Formal, M. Gratzel, *ChemSusChem* 4 (2011) 432–449.
- [2] O. Zandi, B.M. Klahr, T.W. Hamann, *Energy Environ. Sci.* 6 (2013) 634–642.
- [3] M. Mishra, D.-M. Chun, *Appl. Catal. A* 498 (2015) 126–141.
- [4] O. Zandi, T.W. Hamann, *Phys. Chem. Chem. Phys. : PCCP* 17 (2015) 22485–22503.
- [5] S.D. Tilley, M. Cornuz, K. Sivula, M. Gratzel, *Angew. Chem.* 49 (2010) 6405–6408.
- [6] Q. Zeng, J. Bai, J. Li, L. Xia, K. Huang, X. Li, B. Zhou, *J. Mater. Chem. A* 3 (2015) 4345–4353.
- [7] J. Wang, B. Feng, J. Su, L. Guo, *ACS Appl. Mater. Interfaces* 8 (2016) 23143–23150.
- [8] Y. Zhang, S. Jiang, W. Song, P. Zhou, H. Ji, W. Ma, W. Hao, C. Chen, J. Zhao, *Energy Environ. Sci.* 8 (2015) 1231–1236.
- [9] W. Sun, Q. Meng, L. Jing, L. He, X. Fu, *Mater. Res. Bull.* 49 (2014) 331–337.
- [10] C. Liu, X. Li, J. Su, L. Guo, *Int. J. Hydrogen Energy* 41 (2016) 12842–12851.
- [11] Z. Luo, C. Li, S. Liu, T. Wang, J. Gong, *Chem. Sci.* 8 (2017) 91–100.
- [12] A. Srivastav, A. Verma, A. Banerjee, S.A. Khan, M. Gupta, V.R. Satsangi, R. Shrivastav, S. Dass, *Phys. Chem. Chem. Phys. : PCCP* 18 (2016) 32735–32743.
- [13] A. Banerjee, B. Mondal, A. Verma, V.R. Satsangi, R. Shrivastav, A. Dey, S. Dass, *J. Catal.* 352 (2017) 83–92.
- [14] B. Iandolo, B. Wickman, I. Zorić, A. Hellman, *J. Mater. Chem. A* 3 (2015) 16896–16912.
- [15] T.H. Jeon, G.-h. Moon, H. Park, W. Choi, *Nano Energy* 39 (2017) 211–218.
- [16] D.D. Qin, C.H. He, Y. Li, A.C. Trammel, J. Gu, J. Chen, Y. Yan, D.L. Shan, Q.H. Wang, J.J. Quan, *ChemSusChem* (2017).
- [17] L. Xi, P.S. Bassi, S.Y. Chiam, W.F. Mak, P.D. Tran, J. Barber, J.S. Chye Loo, L.H. Wong, *Nanoscale* 4 (2012) 4430–4433.
- [18] T.H. Jeon, A.D. Bokare, D.S. Han, A. Abdel-Wahab, H. Park, W. Choi, *Appl. Catal. B: Environ.* 201 (2017) 591–599.
- [19] S. Shen, J. Zhou, C.L. Dong, Y. Hu, E.N. Tseng, P. Guo, L. Guo, S.S. Mao, *Sci. Rep.* 4 (2014) 6627.
- [20] K.J. McDonald, K.-S. Choi, *Chem. Mater.* 23 (2011) 4863–4869.
- [21] F. Zhang, X. Li, Q. Zhao, D. Zhang, *ACS Sustain. Chem. Eng.* 4 (2016) 4554–4562.
- [22] Q. Liu, F. Cao, F. Wu, W. Tian, L. Li, *RSC Adv.* 5 (2015) 79440–79446.
- [23] Y. Huang, C. Han, Y. Liu, M.N. Nadagouda, L. Machala, K.E. O'Shea, V.K. Sharma, D.D. Dionysiou, *Appl. Catal. B: Environ.* 221 (2018) 380–392.
- [24] C. Chen, H. Bai, Z. Da, M. Li, X. Yan, J. Jiang, W. Fan, W. Shi, *Funct. Mater. Lett.* 08 (2015) 1550058.
- [25] S. Bera, A.A.M. Prince, S. Velmurugan, P.S. Raghavan, R. Gopalan, G. Panneerselvam, S.V. Narasimhan, *J. Mater. Sci.* 36 (2001) 5379–5384.
- [26] Y. Zhang, H. Zhang, H. Ji, W. Ma, C. Chen, J. Zhao, *J. Am. Chem. Soc.* 138 (2016) 2705–2711.
- [27] Y. Deng, M. Xing, J. Zhang, *Appl. Catal. B: Environ.* 211 (2017) 157–166.
- [28] D. Monllor-Satoca, M. Bärtsch, C. Fàbrega, A. Genç, S. Reinhard, T. Andreu, J. Arbiol, M. Niederberger, J.R. Morante, *Energy Environ. Sci.* 8 (2015) 3242–3254.